Crystallization and nanoindentation behavior of a bulk Zr–Al–Ti–Cu–Ni amorphous alloy

J.G. Wang[a)]
Department of Chemical and Biochemical Engineering and Materials Science, University of California, Irvine, California 92697

B.W. Choi and T.G. Nieh
Chemistry and Materials Science, Lawrence Livermore National Laboratory, P.O. Box 808, L-350, Livermore, California 94551-9900

C.T. Liu
Metals and Ceramics Division, P.O. Box 2008, Oak Ridge National Laboratory, Oak Ridge, Tennessee 37831-6376

(Received 26 May 1999; accepted 7 January 2000)

The crystallization and nanoindentation behavior of a Zr–10Al–5Ti–17.9Cu–14.6Ni (at.%) bulk amorphous alloy (BAA) were studied. Resulting from the kinetic nature of phase transformation in multicomponent alloys, the crystallization path is complex. Despite the complexity of different crystallization paths, the main final crystallized product in the Zr-based BAA is Zr_2Cu. Young's modulus and hardness of the BAA were found to increase with an increase in annealing temperature. The observed mechanical properties were correlated with the microstructure of the material. Also, in the present paper, both the observed crystallization and nanoindentation behavior are compared with existing data. Zr-based BAAs exhibit a ratio of hardness to Young's modulus (H/E ratio) of about 1/10, suggesting the interatomic bonding in the alloys is close to being covalent.

I. INTRODUCTION

Bulk amorphous alloys (BAAs) with complex multicomponent chemistry and excellent glass-forming ability have recently been developed.[1,2] The production of these bulk amorphous alloys is the subject of considerable scientific interest because of the promising properties shown by these materials and their possible applications as engineering materials. Several alloy families, for example, La base,[3] Mg base,[4] Zr base,[3,5–8] and Fe base[9] have been developed. Among them, Zr-based BAAs, e.g., Zr–Al–TM,[3,5] Zr–Ti–TM–Be,[6] and Zr–Ti–Al–TM[7,8] are most interesting because of having a broad supercooled liquid region.[10] Zr–10Al–5Ti–17.9Cu–14.6Ni (in at.%, hereafter) is a new BAA composition developed.[11] The effect of oxygen impurity on the undercooling and crystallization kinetics,[11] the influence of testing environment on the room-temperature mechanical properties of this alloy,[12] and the superplastic behavior in the supercooled liquid region[13] have been reported. It was found that the mechanical behavior strongly depends on the microstructure of the material. The presence of a minor amount of crystalline phase can significantly embrittle the alloy. In the present paper, a systematic study of the crystallization behavior and its influence on the nanoindentation behavior of this alloy are carried out.

II. EXPERIMENTAL PROCEDURE

The Zr-based alloy with a nominal composition of Zr–10Al–5Ti–17.9Cu–14.6Ni (at.%) was prepared by arc melting and drop casting, as described previously.[12] The as-cast amorphous samples used in the present study are of a cylindrical shape with a diameter of 7 mm. The amorphous nature of the cast samples was verified by Rigagu's RU300 x-ray diffractometry (XRD), with a rotating anode of Cu as a target material, and transmission electron microscopy (TEM). The thermal properties of the alloy were measured using differential scanning calorimetry (DSC) in a Du Pont 9900 Thermal Analysis System with different heating rates. A typical DSC run involves heating a sample from room temperature to 923 K. The crystallization behavior of the annealed samples was studied by using XRD and TEM. Annealing treatments were carried out *in situ* in the DSC cell with a

[a)]Address all correspondence to this author.
e-mail: wangjg@uci.edu

heating rate of 20 K/min under flowing N_2. TEM specimens were prepared using standard twin-jet electropolishing in a solution containing one part sulfuric acid plus seven parts methanol at −25 °C and then examined using a JEOL-200CX microscope.

Nanoindentation tests were carried on the as-cast and annealed samples with a Nano Indenter XP®. Hardness and elastic modulus were measured using the continuous stiffness option, which yields elastic modulus and hardness as a function of indentation depth.[14] A Berkovich indenter was used in the experiments. Five types of experiments, hardness test at a load, hardness test at a depth, continuous stiffness test at a depth, continuous stiffness at a load, and a four times load/unload experimental procedure,[14] were performed at different loads and depths. Ten indentations were made for each test on each specimen, with most of the results presented here representing averages for the group.

III. EXPERIMENTAL RESULTS

A. As-received BAA

The XRD and TEM results obtained from the as-cast amorphous sample are presented in Fig. 1. The XRD pattern consists of only a broad amorphous peak with a maximum intensity at the wave vector ($K_p = 4\pi\sin\theta/\lambda$) of 26.2 nm^{-1} and no crystalline phases are discernible. The electron-diffraction pattern reveals the presence of a diffuse amorphous ring without any crystalline feature. It is consistent with that reported previously;[12] namely, the as-cast alloy contains essentially no crystalline particles and cast cavity.

B. DSC measurements

The DSC curves of the Zr-based BAA at various heating rates are shown in Fig. 2. The amorphous alloy shows an endothermic reaction caused by the glass transition, followed by a supercooled liquid region and, then, an exothermic reaction caused by crystallization. In the figure, the onset temperatures for the glass transition and crystallization are denoted by T_g and T_x, respectively. As expected, both T_g and T_x increase with an increase in heating rate. The temperature interval between T_g and T_x, i.e., the supercooled liquid region, $\Delta T_x = (T_x - T_g)$, also increases with increasing heating rate, clearly indicating that glass transition and crystallization of the BAA are kinetic processes.[15] Table I summarizes the thermal parameters of T_g, T_x, ΔT_x at different heating rates. These data are in good agreement with the DSC results of Lin *et al.*[11] who reported that at a heating rate of 20 K/s glass transition occurs at temperatures between 682 and 713 K, corresponding to a reduced glass-transition temperature of about 0.64 to 0.66 (melting temperature 1069 K).

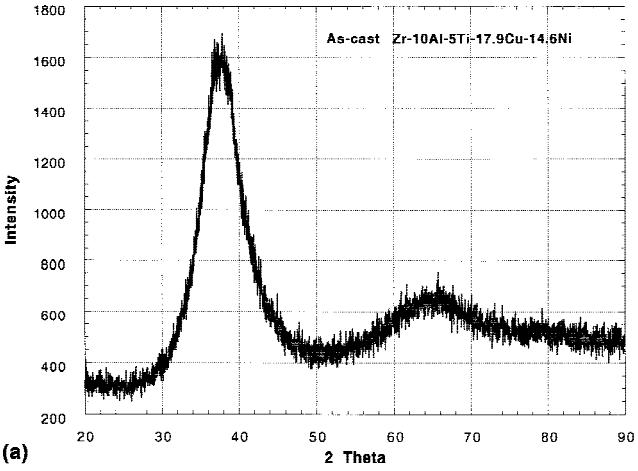

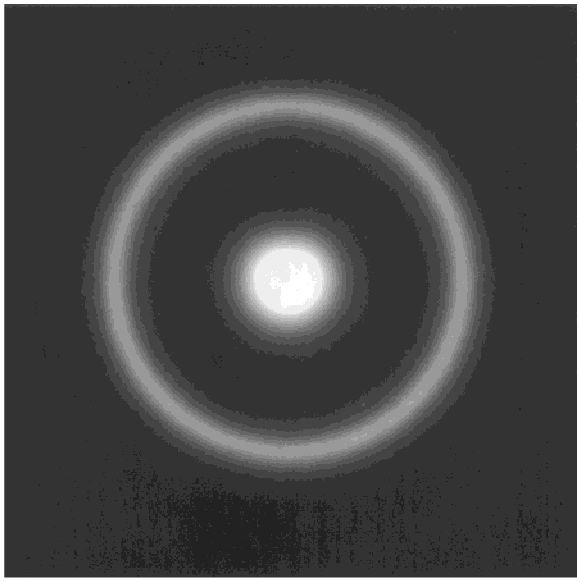

FIG. 1. (a) X-ray and (b) TEM diffraction patterns of the as-cast amorphous $Zr_{52.5}Al_{10}Ti_5Cu_{17.9}Ni_{14.6}$ alloy.

C. Crystallization behavior

Annealing treatment was performed *in situ* in a DSC cell with a heating rate of 0.33 K/s under flowing N_2 to minimize kinetic effects. Annealing temperatures were selected to be 683, 783, and 893 K, corresponding to the supercooled liquid region, after the first crystallization peak, and after the second crystallization peak, in the DSC curves (Fig. 2), respectively. After reaching the predetermined temperatures, the samples were rapidly cooled to room temperature (drops from 923 to 658 K within 600 s after shutting off the electric power). The annealed samples were then examined by XRD. Figure 3 shows the XRD patterns obtained from as-received BAA sample [Fig. 3(a)], samples annealed at 683 K [Fig. 3(b)], 783 K [Fig. 3(c)], and 893 K [Fig. 3(d)], respectively. Also included in Fig. 3(e) is the XRD pattern from a sample annealed at 923 K for 1 h. The 683-K–

annealed sample does not reveal any discernible crystallization, although the diffuse amorphous ring is sharper than that from the as-cast sample. Apparently, the amorphous glass relaxes into a supercooled liquid state. Annealing at 783 K leads to a partial crystallization and the formation of tetragonal Zr_2Ni (space group *I*4/*mcm*, $a = 0.649$ nm, $c = 0.528$ nm) and [Ni,(Zr,Ti)] with a hexagonal structure. It is noted that, at lower cooling rates, e.g., 0.167 and 0.33 K/s, two subpeaks appear and are actually associated with the first crystallization peak in the DSC curve. These two subpeaks may correspond to these two crystalline phases. The formation of primary Zr_2Ni during the crystallization of amorphous $Zr_{60}Al_{10}Cu_{20}Ni_{10}$[8] and $Zr_{55}Al_{10}Cu_{30}Ni_5$[16] has been reported.

Annealing at 893 K results in two additional phases, $Zr(Al,Ni)_2$ and NiZr. $Zr(Al,Ni)_2$ is a metastable phase with a cubic structure (space group *F*d3*m*), and NiZr is an orthorhombic phase with a space group *Cmcm*. Annealing at a higher temperature of 923 K for 1 h produces a fully crystallized sample. The crystallized products include Zr_2Cu (main phase) with a tetragonal structure (space group *I*4/*mmm*, $a = 0.322$ nm, $c = 1.118$ nm), $Ni_{10}Zr_7$ with an orthorhombic structure (space group *A*b2*a*, $a = 0.922$ nm, $b = 1.229$ nm, $c = 0.915$ nm), Al_3Zr_4 with a hexagonal structure (space group *P*6, $a = 0.5432$ nm, $c = 0.5389$ nm), and probably a trace of Zr_2Ni. No appreciable diffraction peaks corresponding to Ti-based compounds are seen. Because Zr and Ti form a complete solid solution over the entire composition range, Ti may have dissolved in a substitutional form in the Zr-based compounds.

A bright-field TEM image and selected-area electron-diffraction pattern of the as-cast sample and samples annealed at different temperature are shown in Fig. 4. Both the as-cast sample and the 683 K–annealed sample show a uniform amorphous microstructure [Fig. 4(a) and Fig. 4(b)]. The halo ring in the diffraction pattern of the 683 K annealed sample is apparently sharper than that of the as-cast sample, as a result of relaxation of the glassy state. In contrast, the samples annealed at 783 and 893 K consist mainly of very fine Zr_2Ni grains with a size of less than 10 nm at 783 K and 40 nm at 893 K [Figs. 4(c) and 4(d)]. The diffraction patterns contain distinct triple rings resulting from the three diffraction peaks of the Zr_2Ni phase. The volume fraction of this nanocrystalline phase is estimated to be 80% at 783 K and 95% at 893 K from TEM images. The microstructure of the sample annealed at 923 K for 1 h, shown in Fig. 4(e), is a polycrystal with an average grain size of about 250 nm. The diffraction pattern consists of spotty reflection rings resulting from the presence of the Zr_2Cu phase; it no longer has the triple ring characteristic of the Zr_2Ni phase.

D. Nanoindentation behavior

Representative load-displacement plots of indentations made at a 6-mN indentation load on the samples annealed at different temperatures are shown in Fig. 5. The experiments were carried out using a typical load-time sequence developed by Oliver and Pharr.[14] The indenter was loaded and unloaded four times in succession at a

TABLE I. Temperatures for the start (T_g^s) and end (T_g^e) of glass transition, crystallization (T_x), and supercooled range (ΔT_x) for amorphous Zr–10Al–5Ti–17.9Cu–14.6Ni alloy.

Heating rates (K/s)	T_g^s, K	T_g^e, K	T_x, K	ΔT_x, K
0.167	628	696	714	86
0.33	631	705	729	98
0.67	637	716	742	105
1.33	640	728	758	118

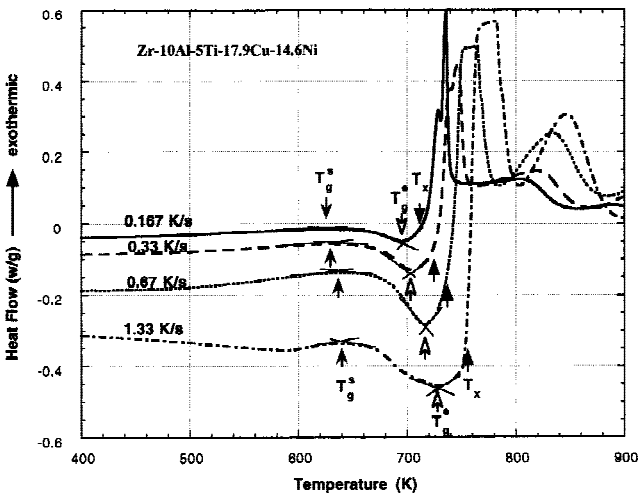

FIG. 2. DSC curves of the Zr-based BAA at various heating rates: (a) 0.167 K/s, (b) 0.33 K/s, (c) 0.67 K/s, and (d) 1.33 K/s.

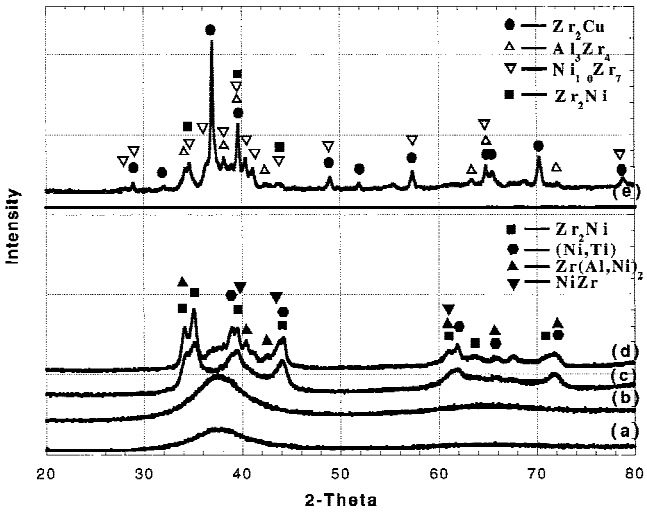

FIG. 3. XRD patterns from as-cast and annealed BAA samples: (a) as received, (b) 683 K, (c) 783 K, (d) 893 K, and (e) 923 K for 1 h.

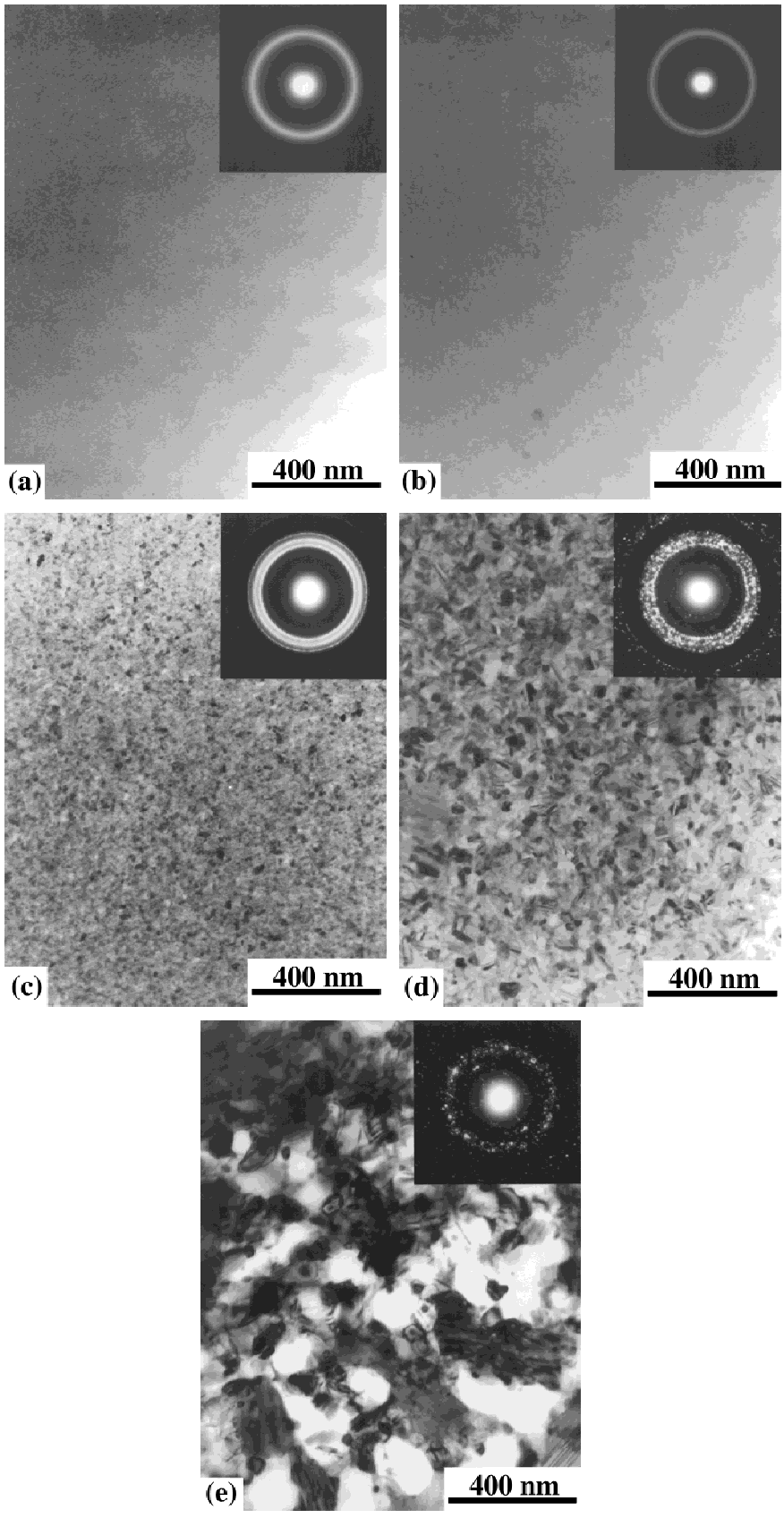

FIG. 4. Bright-field TEM images and selected-area electron-diffraction patterns of the as-cast and annealed BAA samples: (a) as received, (b) 683 K, (c) 783 K, (d) 893 K, and (e) 923 K for 1 h.

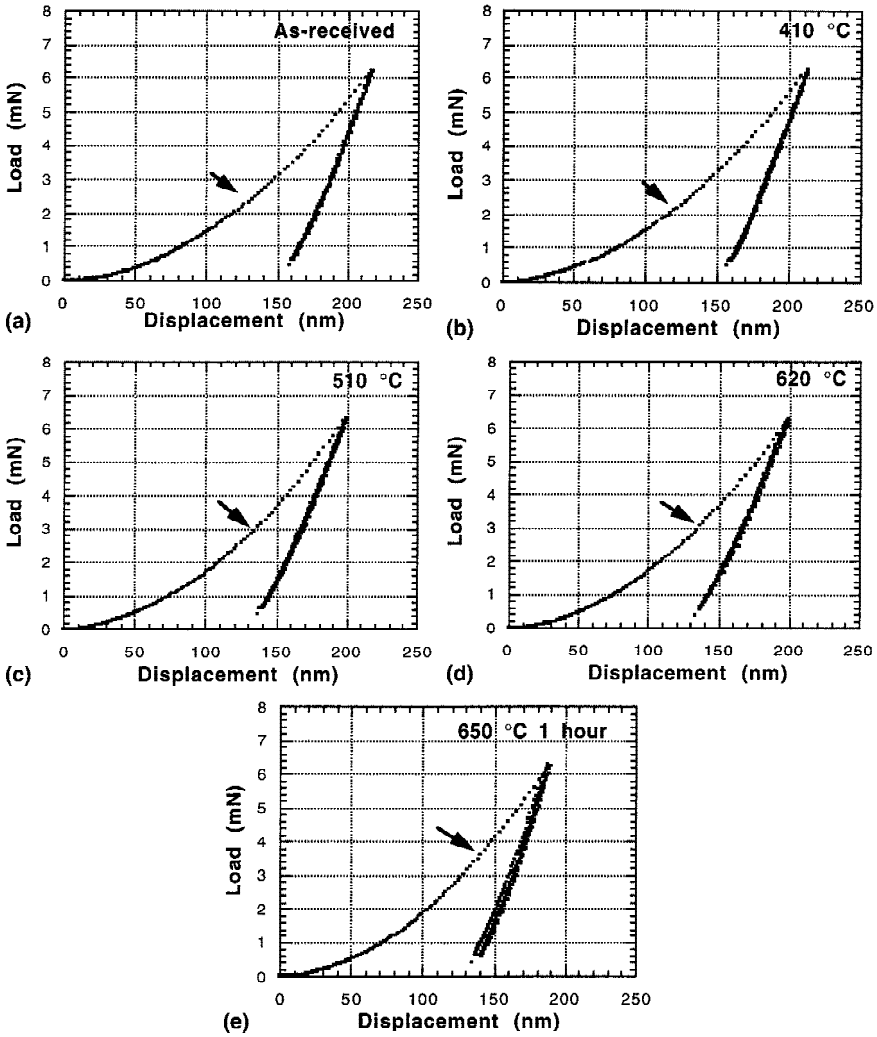

FIG. 5. Representative load-displacement plots for as-received and different-temperature-annealed BAA samples obtained from nanoindentation at 6.0-mN peak indentation load: (a) as received, (b) 683 K, (c) 783 K, (d) 893 K, and (e) 923 K for 1 h. Locations on the loading curve marked by arrows show a displacement discontinuity or pop-in of the tip into material during the loading step in the indentation process.

constant loading rate/load ($1/P\ dP/dt$), because a constant loading rate/load ($1/P\ dP/dt$) results in a constant indentation strain rate ($1/h\ dh/dt$).[17] A lower indentation depth indicates a higher hardness and a higher slope of the unloading curve indicates a higher stiffness or elastic modulus. As shown in Fig. 5, the sample annealed at 923 K exhibits the lowest indentation depth, about 186 nm, as compared to other samples. The shape of load-displacement curves and indentation depths obtained from the as-received sample are essentially the same as from the 683 K annealed sample. The load-displacement curve for the 783 K annealed sample is also similar to that for the 893 K annealed sample.

It is noted that load-displacement plots exhibit several displacement discontinuity or pop-in marks during the first loading of indentation. These pop-in marks indicate a sudden penetration of the tip into the sample. The non-uniform penetration is probably a result of either onset of a sudden plastic deformation or formation of cracks. The load value for the onset of pop-in increases with increasing annealing temperature, suggesting the as-cast material has the lowest resistance to plastic deformation or to crack formation.

Hardness and elastic modulus profiles as a function of indentation depth for the as-cast and annealed samples are shown in Fig. 6. These hardness and elastic modulus are also summarized in Table II. Here, data from two types of nanoindentation test are included: test at a fixed load and test at a fixed depth.

The as-cast BAA sample exhibits the lowest hardness of 6.3 GPa and the lowest elastic modulus of 112 GPa (at a load of 60 mN). In contrast, the sample annealed at 923 K/1h exhibits the highest elastic modulus of 150 GPa and the highest hardness of 8.6 GPa. In general, the hardness increases with increasing annealing temperature, and an increase in annealing temperature also

results in an increased elastic modulus. A close examination of the modulus data shows that the data can be divided into three ranges: the data of as-cast sample (~112 MPa); the data of 683, 783 and 893 K annealed samples (~119 MPa); and the data of 923 K/1h annealed sample (~150 MPa). Evidently, the as-cast sample has a uniform amorphous structure, and the 683 K annealed sample is also amorphous, but in a relaxed state (supercooled liquid). In comparison, the 783 and 893 K annealed samples consist of nanocrystals dispersed in a relaxed amorphous matrix. The 923 K/1h annealed sample is fully crystallized (main phase is Zr_2Cu). The hardness data can also be divided into three groups: the data of as-cast alloy (~6.3 MPa), the data of 683 K annealed sample (~6.9 MPa), and the data of 783, 893, and 923 K/1h annealed samples (~8.6–8.9 MPa). The relaxed amorphous material is slightly harder than the as-cast material, whereas the nanocrystal-containing materials have the highest hardness.

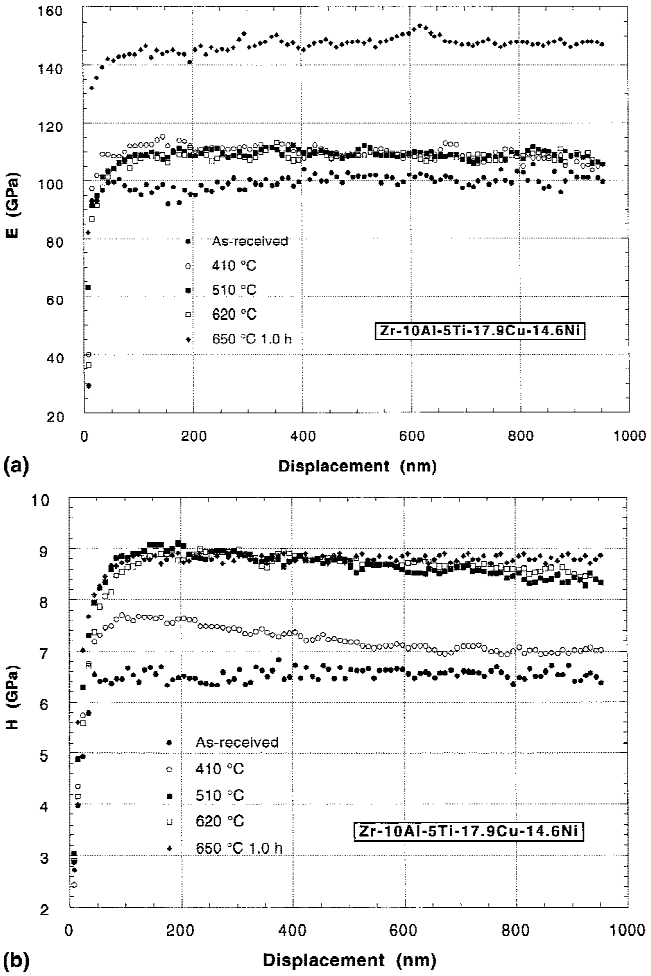

FIG. 6. (a) Elastic modulus and (b) hardness profiles as a function of indentation depth for the as-cast and annealed BAA samples.

TABLE II. Hardness and elastic modulus of as-cast and annealed BAA samples obtained from different nanoindentation test.

Sample	Test[a]	Depth (nm)	Load (mN)	Elastic modulus (GPa)	Hardness (GPa)
As-received	HL	733 ± 4	60	112 ± 6	6.3 ± 0.6
	HD	2000	474 ± 4	92 ± 4	6.2 ± 2
683 K annealed	HL	700 ± 3	60	119 ± 2	6.9 ± 0.1
	HD	2000	496 ± 8	100 ± 5	6.5 ± 0.2
783 K annealed	HL	661 ± 3	60	118 ± 2	8.3 ± 0.1
	HD	2000	590 ± 12	99 ± 4	7.8 ± 0.2
893 K annealed	HL	652 ± 4	60	119 ± 1	8.6 ± 0.1
	HD	2000	604 ± 10	99 ± 4	8.0 ± 0.2
923 K 1 h	HL	627 ± 4	60	150 ± 2	8.6 ± 0.2
	HD	2000	619 ± 17	142 ± 1	8.3 ± 0.1

[a]HL, hardness test at a load; HD, hardness test at a depth.

IV. DISCUSSION

A. Crystallization

Thermal stability and crystallization behavior of several Zr-based BAAs have been examined.[6,8,18,19] Table III lists the reported data of T_g, T_x, and ΔT_x for these Zr-based BAAs. Compared with the base alloys Zr–Al–Cu–Ni,[8,18] any slight alloying addition tends to alter the glass transition and crystallization temperatures. For Ti addition, in particular, T_g, T_x, and ΔT_x all decrease, indicating the bonding among the constituent elements weakens as a result of Ti addition. This is consistent with the experimental results observed in the present study.

Recent results on the crystallization behavior of Zr-based BAAs are summarized in Table IV. As a result of the inclusion of a large number of constituent elements in each alloy, phase formation during crystallization is complex. As expected, the phase formation was strongly affected not only by a specific constituent element, but also by the atomic fraction of the element. For example, the phase structure of the crystallized products can be strongly modified by a small addition of Pd[22] and Ag[18] to the baseline $Zr_{60}Cu_{30}Al_{10}$ or $Zr_{65}Al_{7.5}Ni_{10}Cu_{17.5}$ alloys. Increasing Ti content in a $Zr_{70-x-y}Ti_xAl_yCu_{20}Al_{10}$ alloy can cause the main phase to change from Zr_2Ni to

TABLE III. T_g, T_x and ΔT_x for various Zr-based BAAs.

Composition (at.%)	Heating rate (K/s)	T_g (K)	T_x (K)	ΔT_x (K)	Refs.
$Zr_{41.2}Ti_{13.8}Cu_{12.5}Ni_{10.0}Be_{22.5}$	0.33	625	705	80	6
$Zr_{65}Al_{7.5}Ni_{10}Cu_{17.5}$	0.67	635	746	111	18
$Zr_{65}Al_{7.5}Ni_{10}Cu_{12.5}Ag_5$		660	723	63	
$Zr_{64.8}Al_{7.7}Cu_{18.2}Ni_{9.3}O_{0.2}$	0.33	637	744	107	19
$Zr_{66.1}Al_{7.2}Cu_{17.4}Ni_{9.3}O_{0.4}$		638	732	94	
$Zr_{66.6}Al_{7.2}Cu_{17.2}Ni_{9.0}O_{0.8}$		647	714	67	
$Zr_{55}Al_{15}Cu_{20}Ni_{10}$	0.67	709	805	96	8
$Zr_{55}Ti_{2.5}Al_{12.5}Cu_{20}Ni_{10}$		690	775	85	
$Zr_{55}Ti_5Al_{10}Cu_{20}Ni_{10}$		669	752	83	

TABLE IV. Crystallization behavior of Zr-Based BAAs.

Alloy composition (at.%)	Annealing condition	Crystallization behaviors	Refs.
$Zr_{41}Ti_{13}Cu_{13}Ni_{10}Be_{23}$	>688 K(*in situ* x-ray)	Am→Be_2Zr+$CuZr_2$+CuZr	20
$Zr_{41}Ti_{15}Cu_{12}Ni_{11}Be_{21}$	DSC at 2 K/min	Am→hex+Am′→hex+Tet	21
$Zr_{60}Al_{10}Cu_{30}$	T_x+50K, 900 s	Am→Zr_2Cu+ZrCu+Zr_3Al	16
$Zr_{55}Al_{10}Cu_{30}Ni_5$		Am→Zr_2Cu+ZrCu+Zr_2Ni+Zr_3Al	
$Zr_{60}Cu_{30}Al_{10}$	705 K, 1.2 ks	Am→Zr_2Cu+Zr_2Al	22
$Zr_{55}Cu_{30}Pd_5Al_{10}$	726 K, 3.6ks; 808 K, 900s	Am→Am′+Zr_2(Cu,Pd)→Zr_2(Cu,Pd)+Zr_3(Al,Pd)$_2$	
$Zr_{65}Al_{7.5}Ni_{10}Cu_{17.5}$		Am→Zr_2(Cu,Ni)+Zr_2(Al,Ni)	18
$Zr_{65}Al_{7.5}Ni_{10}Cu_{12.5}Ag_5$	730 K, 180s	Am→Am′+Zr_3(Al,Ag)$_2$	
	750 K, 120s	→Zr_3(Al,Ag)$_2$+Zr_2(Cu,Ni)	
$Zr_{70-x-y}Ti_xAl_yCu_{20}Al_{10}$	T_x+100 K, 3.6ks	Am→Zr_2Ni+ZrCu+Zr_3Al(5~15% Al, 0~2.5% Ti)	8
		Am→ZrNi+Zr_2Cu+Zr_3Al(5~15% Al, 2.5~7.5% Ti)	
$(Zr_{0.65}Al_{0.075}Cu_{0.175}Ni_{0.1})_{100-x}O_x$	~698 K, 1.8ks	Am→Zr_2Cu+Zr_6NiAl_2+qc	19
	~723 K, 1.8ks	→Zr_2Cu+Zr_6NiAl_2+fcc−$NiZr_2$	
	~873 K, 1.8ks	→Zr_2Cu+Zr_6NiAl_2	
$Zr_{57}Cu_{20}Al_{10}Ni_8Ti_5$	0.33 K/s to 720 K, 60s	Am→Zr_2Ni+Zr_2Cu+qc	23
	0.33 K/s to 823 K, 60s	→Zr_2Ni+Zr_2Cu	
	0.33 K/s to 960 K, 60s	→Zr_2Cu+Zr_6NiAl_2	

Zr_2Cu.[8] Even for the same $Zr_{60}Cu_{30}Al_{10}$ alloy, different phases have been observed for different crystallization treatments by the same research group.[16,22] Whereas some authors reported the observation of quasi-crystals during the initial stage of crystallization,[19,23] others did not detect the quasi-crystal-like (qc) phase.[8,16,18,22] Apparently, the exact phases formed during crystallization also strongly depend upon the specific crystallization process. Different annealing treatments result in different reaction paths; thus, different kinds of crystallized phases formed. This may be anticipated because of the highly kinetic nature of amorphous alloys. However, despite the complexity of different crystallization paths, it generally agrees that the main product in the equilibrium, crystallized Zr-based BAAs, is Zr_2Cu. This phase is also observed in the present study (annealing treatment at 923 K for 3600 s).

It is worth noting that diffraction patterns change distinctly from samples annealed at 893 K to samples annealed at 923 K for 1 h. As shown in Fig. 1, the structure consists of Zr_2Ni + Ni(Ti,Zr) + NiZr + $Zr(AlNi)_2$ for the 893-K–annealed sample and Zr_2Cu + Zr_2Ni + $Ni_{10}Zr_7$ + Al_3Zr_4 for the 923-K–annealed sample. The 923 K/1h annealing is regarded as an equilibrium annealing treatment; thus, the crystallized phases are thermodynamic equilibrium phases. The phases present in samples annealed at 783 K and 893 K are, however, metastable. In the present study, the main metastable phase obtained was Zr_2Ni. Similar results have been reported by Xing *et al.*[23] in a $Zr_{57}Cu_{20}Al_{10}Ni_8Ti_5$ alloy. Evidently, there exists a solid reaction causing Zr_2Ni to transform into Zr_2Cu either by annealing at 893 K for a longer period of time or at a higher temperature.

In order to examine the difference in phase formation between the equilibrium and nonequilibrium annealing treatment, an *in situ* annealing treatment was performed in the DSC at 923 K followed by rapid cooling. Figure 7 shows the XRD pattern for this sample. The phases present in the 923-K–annealed sample in Fig. 7 are essentially the same as those observed for the 893 K–annealed sample. The main phase is Zr_2Ni. Apparently, there exists a phase transformation from Zr_2Ni to Zr_2Cu by annealing a sample at 923 K for 1 h. Based on the above, schematic continuous cooling transformation (CCT) curves for the crystallization of the Zr–10Al–5Ti–17.9Cu–14.6Ni alloy were constructed as shown in Fig. 8. Only the main phases Zr_2Ni and Zr_2Cu are considered in the curves. When the sample is heated to 923 K at a heating rate of 0.33 K/s, Zr_2Ni is the initial main phase; after a long period (3600 s) of isothermal annealing, Zr_2Cu phase begins to form and Zr_2Ni phase transforms into Zr_2Cu phase. At the present time, it is impossible to predict the partitioning of each element during the crystallization of a multicomponent metallic glass.

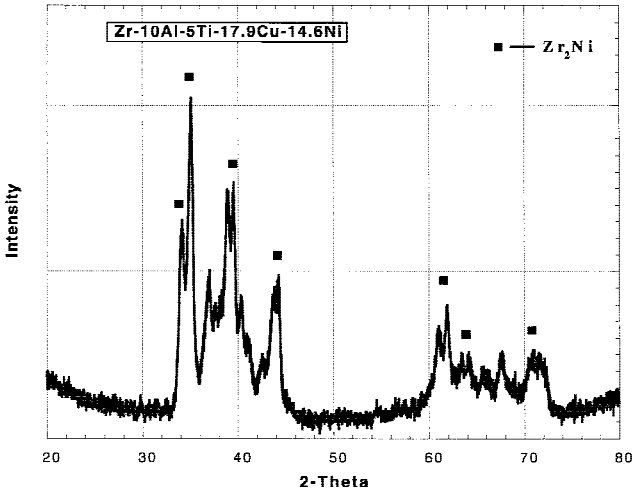

FIG. 7. XRD pattern of a BAA sample annealed at 923 K.

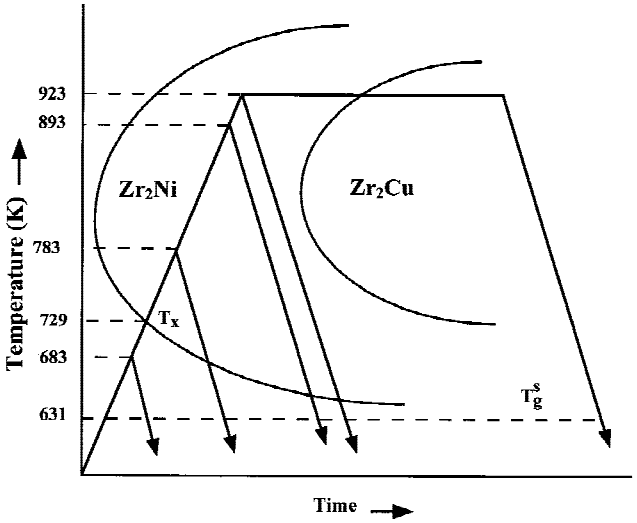

FIG. 8. Schematic CCT curves for the crystallization of the Zr–10Al–5Ti–17.9Cu–14.6Ni alloy.

B. Young's modulus (E) and hardness (H)

Table III summarizes available data on the mechanical properties of Zr-based BAAs, including elastic modulus, hardness, yield strength, fracture strength, and fracture toughness. In comparison with the elastic modulus of 89 MPa determined from the tensile stress-strain curve of $Zr_{52.5}Al_{10}Ti_5Cu_{17.9}Ni_{14.6}$,[12] the data measured by nanoindentation are slightly higher.

The present experimental data (Table II) indicate that material having a crystallized structure has a higher modulus than the material with amorphous structure. Elastic modulus is one of the fundamental properties and is determined essentially by the bonding between atoms. To the first order of approximation (e.g., Lennard–Jones potential), the stiffness or elastic modulus of a material depends upon the interatomic distance. A relaxed structure (e.g., annealed at 683 K) has on an average a shorter interatomic distance (caused by volume decrease) than the as-cast amorphous state. As a result, relaxed structure has a larger modulus than the as-cast amorphous structure. Transient annealing at higher temperatures (783 and 893 K) produces a small volume fraction of metastable crystalline phases dispersed in amorphous matrix, but does not affect appreciably the modulus. After annealing at 923 K for 1 h the entire structure crystallizes and the crystallized alloy exhibits a high modulus. It is known that alloy with a crystallized structure usually has a higher modulus than its amorphous counterpart.[29] This has been demonstrated in $Zr_{41}Ti_{13}Ni_{10}Cu_{13}Be_{23}$,[20] $Zr_{55}Al_{10}Ni_5Cu_{30}$,[10] and $Zr_{65}Al_{10}Ni_{10}Cu_{15}$[27] amorphous alloys.

Hardness is a measure of a material's resistance to plastic deformation. In the case of crystalline solids, hardness is directly related to the yield strength of a material. The yield strength of a crystalline solid is determined by dislocation interaction with lattice defects such as vacancy, solute, dislocation, and boundary interfaces. In the case of amorphous alloys, although the exact atomic mechanisms for plastic deformation are unclear, an empirical relationship exists between hardness H and fracture strength σ_f (i.e., $H/\sigma_f \approx 3$).[30]

For the present BAA, partially and fully crystallized materials have the highest hardness, followed by the material with relaxed structure, and the as-cast material is the softest. The fully crystallized material essentially contains nanocrystalline grains. Grain-size strengthening (e.g., Hall–Petch relationship) is expected to dominate. In the partially crystallized materials, on the other hand, a strengthening mechanism, which is similar to dispersion strengthening occurring in crystalline solids, is expected to take place. In fact, Inoue and colleagues[18,22] recently demonstrated that the dispersion of nanometer crystalline particles in amorphous structure can cause a significant increase in hardness. For example, the hardness of an amorphous Zr–Al–Ni–Cu–Ag alloy is 6.3 MPa but increases to 8.6 MPa when the alloy partially crystallizes and contains nanometer crystals. It is unclear why the relaxed structure is slightly harder than the as-cast amorphous structure. Presumably, the as-cast structure contains a higher defect density and residual stresses, and thus is harder than the relaxed structure. However, the data show the opposite. It could be related to more dense packing after relaxation. Without knowing the exact plastic flow mechanisms in amorphous alloys, it is impossible to offer an explanation for the discrepancy at the present time.

Whang *et al.*[31] demonstrated that there is a linear correlation between hardness and modulus. The ratio of H/E for Zr-BAAs listed in Table V varies from 0.047 to 0.096. It is of interest to know that a covalently bonded solid exhibits a higher H/E than that of a metal; the H/E ratio is about 1/10 for most covalently bonded materials, as compared to about 1/500 for face-centered-cubic metals.[32,33] This difference is a result of the fact that plastic yielding in covalent materials involves actual breakage of atomic bonds, a process that requires high stress. In contrast, the low resistance to plastic flow relative to the modulus in metals is attributed to the ease of dislocation slip in these materials. The Zr-based BAAs exhibit an H/E ratio close to 0.1, thereby suggesting that plastic flow is relatively difficult in these materials. Also, the bonding tendency of Zr-BAAs is probably covalent.

V. CONCLUSIONS

The crystallization and nanoindentation behavior of the as-cast Zr–10Al–5Ti–17.9Cu–14.6Ni (at.%) BAA and material annealed at different temperatures has been characterized. The relationship between the microstruc-

TABLE V. Summary of available mechanical properties of Zr-based BAAs.

Alloy composition (at.%) and microstructure	Mechanical properties[a]				Refs.
	E (GPa)	H (GPa)	Other properties	H/E	
$Zr_{41.25}Ti_{13.75}Ni_{10}Cu_{12.5}Be_{22.5}$(Am)	93 ± 1		$\nu = 0.387$, $\sigma_s = 1.87 \sim 2.12$		24
$Zr_{41.25}Ti_{13.75}Ni_{10}Cu_{12.5}Be_{22.5}$(Am)	96	5.2	$\mu = 34.3$, $\nu = 0.36$ $\sigma_s = 1.9$, $K_{IC} = 57$	0.054	25
$Zr_{60}Cu_{20}Pd_{10}Al_{10}$ (Am)	52.2	5.0	$\sigma_f = 1.64$	0.096	22
$Zr_{60}Cu_{20}Pd_{10}Al_{10}$ ($V_f = 75\%$)	62.3	5.9	$\sigma_f = 1.91$	0.095	
$Zr_{65}Al_{7.5}Ni_{10}Cu_{12.5}Ag_5$ (Am)		4.4	$\sigma_f = 1.15$		18
$Zr_{65}Al_{7.5}Ni_{10}Cu_{12.5}Ag_5$ ($V_f = 14\%$)		4.7	$\sigma_f = 1.52$		
$Zr_{55}Al_{10}Ni_5Cu_{30}$ (Am)	103	4.8	$\sigma_f = 1.82$	0.047	26
$Zr_{70-x-y}Ti_xAl_yCu_{20}Ni_{10}$		4.7–5.1	$\sigma_f = 1.55$–1.85		8
$Zr_{41}Ti_{13}Ni_{10}Cu_{13}Be_{23}$ (Am)	88	5.5		0.062	20
$Zr_{41}Ti_{13}Ni_{10}Cu_{13}Be_{23}$ (Cryst.)	116	9.5			
$Zr_{55}Al_{10}Ni_5Cu_{30}$ (Am)	78–80		$\sigma_f = 1.42$–1.57		10
$Zr_{55}Al_{10}Ni_5Cu_{30}$ (Cryst. + Am)	117		$\sigma_f = 0.93$		
$Zr_{65}Al_{10}Ni_{10}Cu_{15}$ (Am)	80		$\sigma_f = 1.52$		27
$Zr_{65}Al_{10}Ni_{10}Cu_{15}$ (Cryst. + Am)	117		$\sigma_f = 0.93$		
$Zr_{60}Al_{10}Co_3Ni_9Cu_{18}$ (Am)	97	4.7	$\sigma_f = 1.51$	0.048	28
$Zr_{57}Ti_5Al_{10}Ni_8Cu_{20}$ (Am)			$\sigma_s = 1.54$, $\sigma_f = 1.69$		23
$Zr_{52.5}Al_{10}Ti_5Cu_{17.9}Ni_{14.6}$	89		$\sigma_f = 1.65$–1.88		12
$Zr_{52.5}Al_{10}Ti_5Cu_{17.9}Ni_{14.6}$	92–112	6.2–6.3		0.056~0.067	This study

[a]E, elastic modulus; μ, shear modulus (GPa); ν, Poission's ratio; H, hardness; σ_s, yield strength (GPa); σ_f, fracture strength (GPa); K_{IC}, fracture toughness (Mpa $\sqrt{m}$); V_f, volume percentage of crystalline particles.

ture and mechanical properties has been discussed. This study has led to the following conclusions:

(1) The crystallization sequence of the BAA with increasing temperatures is as follows:

$$\mathrm{Am} \xrightarrow{683\ \mathrm{K}} \mathrm{Am}' \xrightarrow{783\ \mathrm{K}} \mathrm{Am}' + \mathrm{NiZr_2} + (\mathrm{Ni, (Zr, Ti)}) \xrightarrow{893/923\ \mathrm{K}} \mathrm{Am}' + \mathrm{NiZr_2} + (\mathrm{Ni, (Zr, Ti)}) + \mathrm{Zr(AlNi)_2} + \mathrm{NiZr} \xrightarrow{923\mathrm{K}\ 1\mathrm{h}} \mathrm{Zr_2Cu} + \mathrm{Al_3Zr_4} + \mathrm{NiZr_2} + \mathrm{Ni_{10}Zr_7} \quad .$$

(2) Resulting from the kinetic nature of phase transformation in multicomponent alloys, the crystallization path was complex. Despite the complexity of different crystallization paths, the main final crystallized product in the Zr-based BAA is Zr_2Cu. A phase transformation from Zr_2Ni to Zr_2Cu occurs during long-period isothermal annealing treatment at relatively higher temperature.

(3) Young's modulus and hardness of the BAA increase with an increase in annealing temperature, from Am to supercooled liquid Am′, to partially crystallized, and to fully crystallized, in an ascending order.

(4) Zr-based BAAs exhibit an H/E ratio of about 1/10, suggesting the interatomic bond in the alloys is close to being covalent.

ACKNOWLEDGMENT

This work was performed under the auspices of the United States Department of Energy by Lawrence Livermore National Laboratory under Contract No. W-7405-Eng-48.

REFERENCES

1. A. Inoue, Mater. Trans., JIM **36,** 866 (1995).
2. W.L. Johnson, Mater. Sci. Forum **225–227,** 35 (1996).
3. A. Inoue, T. Zhang, and T. Masumoto, Mater. Trans., JIM **31,** 177 (1990).
4. A. Inoue, T. Nakamura, N. Nishiyama, and T. Masumoto, Mater. Trans., JIM **33,** 937 (1992).
5. T. Zhang, A. Inoue, and T. Masumoto, Mater. Trans., JIM **32,** 1005 (1991).
6. A. Peker and W.L. Johnson, Appl. Phys. Lett. **63,** 2342 (1993).
7. A. Inoue, T. Shibata, and T. Zhang, Mater. Trans., JIM **36,** 1420 (1995).
8. T. Zhang and A. Inoue, Mater. Trans., JIM **39,** 857 (1998).
9. A. Inoue and J.S. Gook, Mater. Trans., JIM **36,** 1180 (1995).
10. A. Inoue, Sci. Rpt. RITU, **A42,** 1 (1996).
11. X.H. Lin, W.L. Johnson, and W.K. Rhim, Mater. Trans., JIM **38,** 473 (1997).
12. C.T. Liu, *et al.*, Metall. Mater. Trans. A, **29A,** 1811 (1998).
13. T.G. Nieh, T. Mukai, C.T. Liu, and J. Wadsworth, Scr. Mater. **40,** 1021 (1999).
14. W.C. Oliver and G.M. Pharr, J. Mater. Res. **7,** 1564 (1992).
15. R. Busch, Y.J. Kim, and W.L. Johnson, J. Appl. Phys. **77,** 4039 (1995).
16. A. Inoue, T. Negishi, H.M. Kimura, T. Zhang, and A.R. Yavari, Mater. Trans., JIM **39,** 318 (1998).
17. B.N. Lucas, W.C. Oliver, G.M. Pharr, and J-L. Loubet, in *Thin Films: Stresses and Mechanical Properties VI*, edited by W.W. Gerberich, H. Gao, J-E. Sundgren, and S. Baker (Mater. Res. Soc. Symp. Proc. **436,** Pittsburgh, PA, 1996) pp. 233.
18. A. Inoue, T. Zhang, and Y.H. Kim, Mater. Trans., JIM **38,** 749 (1997).
19. J. Eckert, N. Mattern, M. Zinkevitch, and M. Seidel, Mater. Trans., JIM **39,** 623 (1998).
20. H.J. Fecht, Philos. Mag. B **76,** 495 (1997).
21. S. Spriano, C. Antonione, R. Doglione, L. Battezzati, S. Crdoso, J.C. Soares, and M.F. da Silva, Philos. Mag. B **76,** 529 (1997).
22. C. Fan and A. Inoue, Mater. Trans., JIM **38,** 1040 (1997).

23. L.Q. Xing, J. Eckert, W. Loser, and L. Schultz, Appl. Phys. Lett. **73,** 2110 (1998).
24. H.A. Bruck, T. Christman, A.J. Rosakis, and W.L. Johnson, Scr. Metall. Mater. **30,** 429 (1994).
25. R.D. Conner, A.J. Rosakis, W.L. Johnson, and D.M. Owen, Scr. Mater. **37,** 1373 (1997).
26. H. Kato and A. Inoue, Mater. Trans. JIM **38,** 793 (1997).
27. Y. Kawamura, H. Kato, A. Inoue, and T. Masumoto, Appl. Phys. Lett. **67,** 2008 (1995).
28. A. Inoue, T. Zhang, and T. Masumoto, Mater. Trans. JIM **36,** 391 (1995).
29. T.C. Chou, T.G. Nieh, S.D. McAdams, and G.M. Pharr, Scr. Metall. Mater. **25,** 2203 (1991).
30. H. Kimura and T. Masumoto, in *Amorphous Metallic Alloys*, edited by F.E. Luborsky (Butterworths, London, United Kingdom, 1983), p. 187.
31. S.H. Whang, D.E. Polk, and B.C. Giessen, in *Proceedings of the Fourth International Conference on Rapidly Quenched Metals*, edited by T. Masumoto and K. Suzuki (Japan Institute of Metals, 1982, 1981), p. 1365.
32. J.J. Gilman, in *The Science of Hardness Testing and Its Research Applications*, edited by Westbrook and Conrad (American Society for Metals, Metals Park, OH, 1973), p. 51.
33. J.J. Gilman, J. Appl. Phys. **46,** 1435 (1975).